Modulating built-in electric field *via* variable oxygen affinity for robust hydrogen evolution reaction in neutral media

Lingling Zhai[1], Xiaojie She[1], Lyuchao Zhuang[1], Yanyong Li[1], Ran Ding[1], Xuyun Guo[1], Yongqi Zhang[2], Ye Zhu[1], Kun Xu[3*], Hong Jin Fan[4*], Shu Ping Lau[1*]

1 Department of Applied Physics, The Hong Kong Polytechnic University, Hung Hom, Hong Kong, P. R. China

2 Yangtze Delta Region Institute (Huzhou) & Institute of Fundamental and Frontier Science，University of Electronic Science and Technology of China, Huzhou 313001, P.R. China

3 School of Chemistry and Chemical Engineering, Key Laboratory of Functional Inorganic Material Chemistry of Anhui Province, Anhui University, Hefei 230601, P. R. China

4 School of Physical and Mathematical Sciences, Nanyang Technological University, Singapore 637371, Singapore

[*] Corresponding author.

Email address: apsplau@polyu.edu.hk (S.P. Lau); fanhj@ntu.edu.sg (H.J. Fan); kunxu@ahu.edu.cn (K. Xu)

Abstract

Work function strongly impacts the surficial charge distribution, especially for metal-support electrocatalysts when a built-in electric field (BEF) is constructed. Studying the correlation between work function and BEF is crucial for understanding the intrinsic reaction mechanism. Herein, we present a Pt@CoO$_x$ electrocatalyst with large work function difference ($\Delta\Phi$) and strong BEF, which shows outstanding hydrogen evolution activity in a neutral medium with a 4.5-fold mass activity higher than 20% Pt/C. Both experimental and theoretical results confirm the interfacial charge redistribution induced by the strong BEF, thus subtly optimized hydrogen and hydroxide adsorption energy. This work not only provides fresh insights into the neutral hydrogen evolution mechanism but also proposes new design principles toward efficient electrocatalysts for hydrogen production in a neutral medium.

Introduction

Hydrogen (H_2) is a crucial feedstock in the industrial production of basic organic chemicals through petroleum refining (*e.g.*, hydrogenation and hydrocracking).[1] In consideration of the environmental issues caused by steam reforming, the electrocatalytic production of hydrogen from renewable sources is raised compellingly.[2] Hydrogen evolution reaction (HER) is applicable in either acidic,[3] alkaline,[4] or neutral media. However, despite some encouraging progress, the corrosive and environmental issues caused by acidic or alkaline electrolytes largely impede their scalable deployment in sustainable energy supplies. Conversely, neutral media compromise these problems due to their benign and harmless properties, which makes neutral HER highly promising.

Unfortunately, in neutral media, the absorbed hydrogen (H^*) source comes from water dissociation ($H_2O + e^- \rightarrow H^* + OH^-$),[5] the sluggish reaction kinetic drives platinum (Pt) exhibiting two to three orders of magnitude lower activity than that in acidic.[6] Clearly, the water dissociation reaction includes two key intermediates: hydrogen and hydroxide. Recent evidence suggests that hydroxide also plays a significant role in the HER pathway.[7] To improve the catalytic performance, one promising strategy is by constructing a metal-support interface, where the metal adsorb hydrogen[6a, 8] and the metal oxides/hydroxides to promote water dissociation and act as active sites to adsorb hydroxide intermediates efficiently.[9] For example, a Pt/NiO nanocomposite reveals excellent catalytic activity for HER, with a mass activity of 15.2 times higher than that of commercial Pt/C at -0.05 V *vs*. RHE. The further theoretical calculation reveals an improved water dissociation and OH^* desorption process than Pt alone.[9] Besides, Pt/TiO$_2$ is also reported as an efficient HER catalyst in both experiment[10] and theory,[11] of which the charge transfer orientation and hydrogen coupling activity are regarded as essential factors. However, when constructing a metal-oxide interface, the electronic structure of both sides would be strongly affected. The overlap of the electron cloud

3

across the interface would drive charge carriers to experience severe localization. Since the proton remains confined inside the oxide, whereas the electron is completely delocalized throughout the metal,[12] such local confinement would largely reduce the BEF. The BEF is created when two substances are contacted to form a heterojunction,[13] the interfacial space charge and band bending tend to separate electrons and protons,[12b] thus alter the charge distribution and affect either hydrogen or hydroxide adsorption.[14] To overcome these limitations, the creation of an interfacial driving force to control the BEF and potential gradients is particularly imperative.

Work function (Φ), defined as the minimum energy needed to remove an electron from Fermi level to the vacuum level,[15] is one of the most fundamental surface properties of a material. By tuning the $\Delta\Phi$ between metal and support, the charge transport orientation across the interface can be controlled.[16] Consequently, the BEF would be affected, thereby modulating the hydrogen and hydroxide adsorption. However, rare cases are reported based on this conception due to the lack of fundamental understandings of the critical factors of $\Delta\Phi$, also the relationship between the BEF and the hydrogen/hydroxide reaction process. Therefore, it is highly desirable to explore further the strong correlation between $\Delta\Phi$ and BEF and its effect on catalytic activity, thus promoting the design of efficient HER electrocatalysts.

Herein, we take a series of Pt-based metal-support catalysts as proof of concept to systematically investigate the intrinsic corelation between Φ and BEF, which optimizes the adsorption energies of hydrogen/hydroxide. Specially, we employ a scarifying agency (Cu) with strong oxygen affinity to precisely control the oxidation state of cobalt oxide (CoO_x), which strongly affects the $\Delta\Phi$ with Pt. As a result, the $Pt@CoO_x$ with a large $\Delta\Phi$ shows an enhanced BEF as evidenced by various electrical characterizations. Furthermore, spectroscopic investigations and theoretical simulations verify that the enhanced BEF plays a crucial role in subtly engineering H* and OH* adsorption strength, which is essential for neutral HER. As a

4

result, the Pt@CoO$_x$ porous nanosheets reveal remarkable HER performance with a low overpotential of 82 mV at a current density of 10 mA cm^{-2} in the neutral electrolyte. The mass activity is 4.5-fold higher than that of 20% Pt/C. This work sheds mechanistic insights into the atomic-level steering of charge flow, and the optimizing strategy may pave new ways to design highly efficient electrocatalysts.

Results and Discussion

Due to the tunable adhesive force, Cu foil is widely adopted for 2D materials (e.g., graphene) growth.[17] By applying ammonium persulfate solution (APS) *via* chemical etching method, the product can be easily transferred. Therefore, it is reasonable to modulate the surface property of Cu foil by adjusting the etching duration, then optimize the contact interface. In this work, Cu foil was adopted as a substrate, the porous Pt@CoO$_x$ nanosheets were synthesized by a coupled electro-thermal method as illustrated in **Figure 1a**. The photo of the samples presenting different stages is given in **Figure S1**. The pristine Cu foil was firstly etched by APS, then the surface was covered by Cu(OH)$_2$ needles and flowers (**Figure S2-S3)**. The corresponding reaction equation is: $Cu + 4NaOH + (NH_4)_2S_2O_8 \rightarrow Cu(OH)_2 + 2Na_2SO_4 + 2NH_3 + 2H_2O$.[18] X-ray diffraction (XRD) characterization also confirms the phase of Cu(OH)$_2$ (**Figure S4**). Then after electroreduction, a rough surface is obtained, as shown in **Figure S5**. For better illustration, the Cu after electroreduction is denoted as Cu-ER. To further confirm the compositional change, the XRD measurement was conducted. As given in **Figure S6a**, the XRD pattern of the Cu-ER matches well with the cubic Cu phase (PDF #65-9026) without detectable peaks from Cu$_2$O, indicating the complete reduction of Cu(OH)$_2$. It should be noted that the peaks at 45.4° and 48.3° come from the impurities in the pristine Cu foil, which have been normally found and reported before.[19] Interestingly, the relative peak intensity ratio (I$_1$/I$_2$)

of (111) and (200) decreases from 3.33 to 0.0057 (**Figure S6b**), indicating completely different surficial properties.

Indeed, such phase change alters the hydrophobic Cu into hydrophilic. As shown in **Figure 1b**, the contact angle reduced from 99.0° to 11.6° after the electroreduction. Moreover, the surface energies of (111) and (200) (**Figure S7**) were calculated to be 0.072 and 0.094 eV/Å^2, respectively, consisting with previous literatures.[20] The higher surface energy indicates a stronger molecular attraction and possible dangling bonds, which may facilitate electrostatic adhesion.[20b] Apparently, such property is crucial for the following electrodeposition process. As shown in **Figure S8**, after electrodeposition, the Cu-ER is covered by a layer of $Co(OH)_2$. Subsequently, the product was calcinated under argon (Ar) atmosphere and characterized by XRD measurement. Surprisingly, the XRD pattern reveals mixed phases of Co_3O_4 and Cu_2O (**Figure S9**). Since the substrate is metallic Cu^0, and the calcination is conducted under an inert environment, we presume that the highly active Cu-ER may plunder oxygen from $Co(OH)_2$ then generate Cu_2O. This oxygen-pillage strategy may lead to oxygen deficiency and a low valence state of Co, which have been widely reported to accelerate the electrocatalytic process.[21] In addition, scanning electron microscope (SEM) images (**Figure S10**) show the hierarchical order with Cu as substrate and CoO_x grown as nanosheet arrays. Finally, Pt nanoparticles were deposited on the Co_3O_4 nanosheet through a magnetron sputtering procedure. The as-prepared sample is denoted as $Pt@CoO_x$.
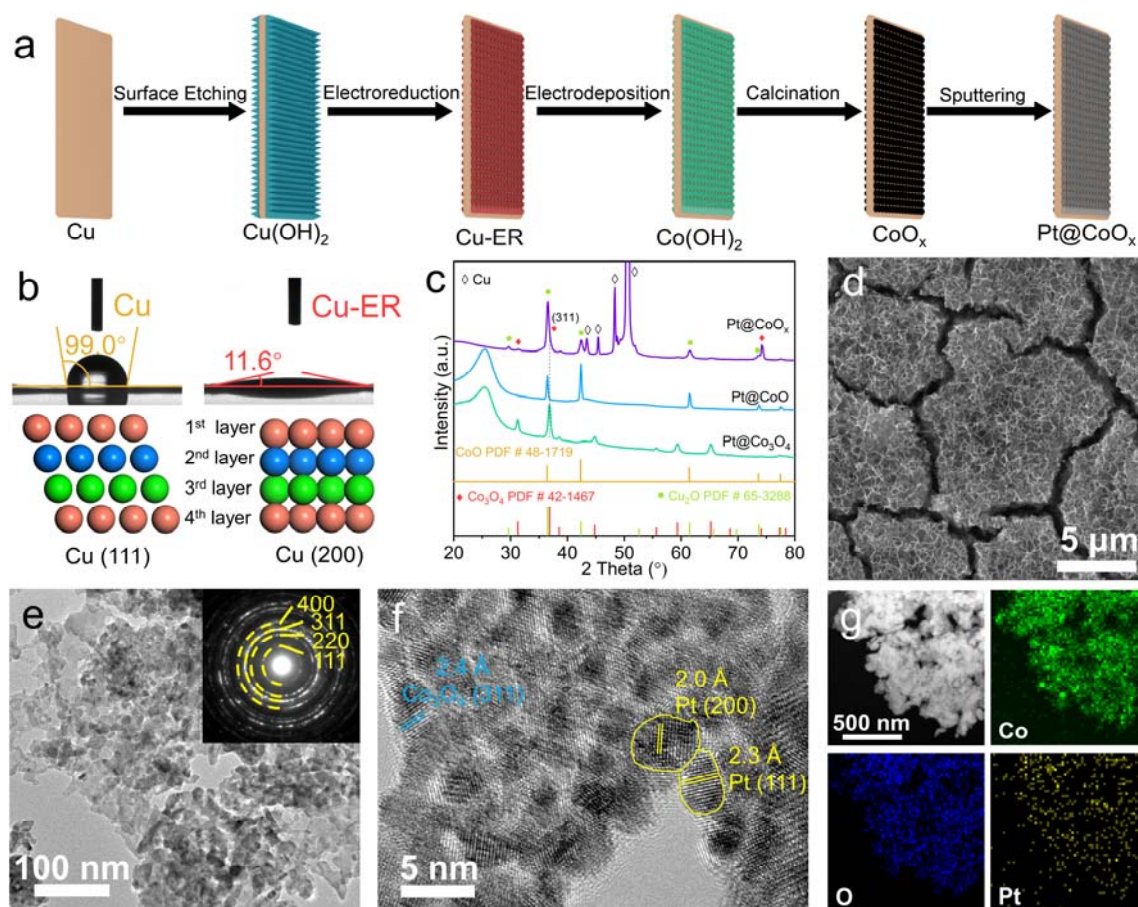
Figure 1. (a) Schematic illustration of the synthesis of Pt@CoO$_x$. (b) Contact angle measurement of Cu and Cu-ER, and the corresponding sideview structure of Cu (111) and Cu (200), respectively. (c) XRD patterns of Pt@Co$_3$O$_4$, Pt@CoO and Pt@CoO$_x$. (d) SEM image of as-prepared Pt@CoO$_x$ nanosheets. (e) TEM image and corresponding SAED pattern of the Pt@CoO$_x$ nanosheet. (f) HRTEM image presenting both Pt nanoparticles and CoO$_x$ nanosheets. (g) EDX mapping of one Pt@CoO$_x$ nanosheet.

To comprehensively investigate the interaction between Pt and cobalt oxide, Pt@CoO and Pt@Co$_3$O$_4$ were prepared using carbon cloth (CC) as substrates (Note: carbon cloth is basically inert, so cobalt oxide almost without oxygen vacancy can be easily realized). The XRD patterns are shown in **Figure 1c**. The Pt@CoO and Pt@Co$_3$O$_4$ exhibit typical phases of cubic CoO (PDF #48-1719) and Co$_3$O$_4$ (PDF #42-1467), respectively. Whereas the Pt@CoO$_x$ shows mixed phases of both Co$_3$O$_4$ and Cu$_2$O (PDF #65-3288), the peak at 36.6 ° presents an overlap of Cu$_2$O (111) and Co$_3$O$_4$ (311). No characteristic peak of Pt is revealed, demonstrating the low concentration and rarely detectable domains. The morphology characterization was further conducted by SEM measurement. As shown in **Figure 1d**, the morphology of Co$_3$O$_4$ nanosheets is well preserved after Pt sputtering. The disordered nanosheets generated multiple

holes and channels, which may contribute to charge transfer and absorbent transportation. The mass concentration of Pt was determined to be ~3.48% by the corresponding energy dispersive X-ray (EDX) spectrum (**Figure S11**). Additionally, the mass loading of Pt was also measured by Inductively Coupled Plasma Optical Emission Spectroscopy (ICP-OES) to be 21.9 μg cm^{-2}. The detailed microstructure of Pt@CoO$_x$ was further studied by transmission electron microscopy (TEM), as shown in **Figure 1e**. As indicated, the nanosheet exhibits a porous morphology composed of numerous interconnected nanocrystals. The corresponding selected area electron diffraction (SAED) pattern also reflects typical planes of (111), (220), (311), and (400) for Co$_3$O$_4$, in good agreement with the XRD result. In addition, the high-resolution TEM (HRTEM) image in **Figure 1f** presents the decoration of Pt nanoparticles with ~ 3 nm. The resolved lattice distances of 2.0 and 2.3 Å match well with the (200) and (111) planes of Pt, consistent with Pt@Co$_3$O$_4$ and Pt@CoO (**Figure S12**). EDX maps in **Figure 1g** further reveals the homogeneous distribution of Co, O, and Pt elements.
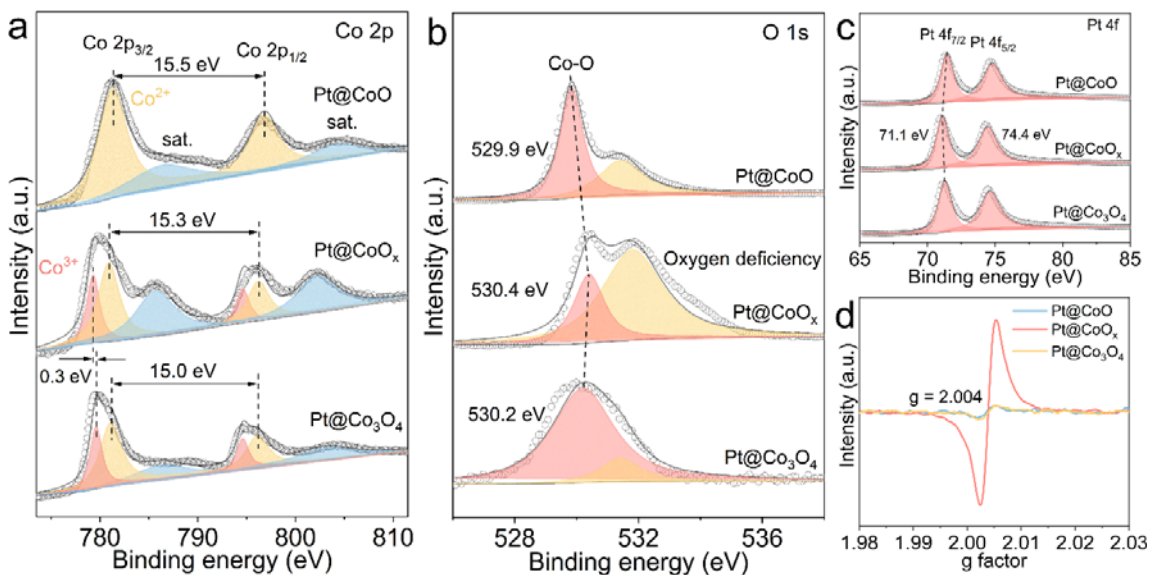
Figure 2. (a) Co 2p, (b) O 1s and (c) Pt 4f XPS spectra of Pt@Co$_3$O$_4$, Pt@CoO$_x$ and Pt@CoO. (d) EPR spectra of Pt@Co$_3$O$_4$, Pt@CoO$_x$ and Pt@CoO.

Furthermore, X-ray photoelectron spectroscopy (XPS) characterization was conducted (see survey spectra in **Figure S13**; the deconvoluted results are summarized in **Table S1-3**). As shown in **Figure S14**, the pristine Co_3O_4 shows Co 2p spectrum at 780.2 eV and 795.4 eV, matching well with previous reports.[22] The deconvoluted Co 2p peak is downshifted by 0.1 eV for $Pt@Co_3O_4$, indicating charge redistribution across the Pt/Co_3O_4 interface. To further evaluate the effect of oxidation state on Co, XPS spectra of $Pt@CoO_x$ and $Pt@CoO$ were also collected (**Figure 2a**). Compared with $Pt@Co_3O_4$ and $Pt@CoO$, the deconvoluted Co 2p peak of $Pt@CoO_x$ is downshifted by 0.2 and 0.4 eV, respectively, verifying an increased oxidation state.[22b] Specifically, the binding energy of Co^{3+} peak (779.3 eV) in $Pt@CoO_x$ is downshifted by 0.3 eV, the doublet separation energy also increases from 15.0 to 15.3 eV. The splitting energy is known to be due to the spin-orbit coupling, so the enlarged splitting value manifests intense electron interaction.[23] Similarly, the O 1s spectrum of $Pt@CoO_x$ is also significantly different from either $Pt@Co_3O_4$ or $Pt@CoO$. As shown in **Figure 2b**, the deconvoluted O 1s peak consists of two peaks located at 530.4 and 531.8 eV representing the lattice oxygen (Co-O) and oxygen deficiency, respectively.[10, 22b] The Co-O binding energy is upshifted by 0.2 eV compared with $Pt@Co_3O_4$, signifying deteriorated electronegativity. Notably, the relative ratios of oxygen deficiency over lattice oxygen, estimated by comparing the fitted peak area, dramatically increased from 0.16 to 2.56, confirming the high degree of oxygen vacancy. The XPS spectra of Pt were also collected as shown in **Figure 2c**. The Pt 4f spectrum of $Pt@CoO_x$ presents two peaks located at 71.1 and 74.4 eV, which belongs to metallic Pt.[24] Moreover, the position is downshifted by 0.2 and 0.3 eV compared with $Pt@Co_3O_4$ and $Pt@CoO$, respectively, manifesting strong electron acquisition. To reconfirm the oxygen deficiency in $Pt@CoO_x$, electron paramagnetic resonance (EPR) was conducted. As shown in **Figure 2d**, the intensity of oxygen vacancies in $Pt@CoO_x$ is much higher than that in both $Pt@Co_3O_4$ and $Pt@CoO$, demonstrating the oxygen deficiency was induced by the intrinsic insufficiency in CoO_x rather

than Pt deposition. Overall, the shift of binding energy in Co, O, or Pt implies robust charge reconstruction on the metal-support interface, which attributes to the variable oxygen affinity, therefore, alters the magnitude of BEF.
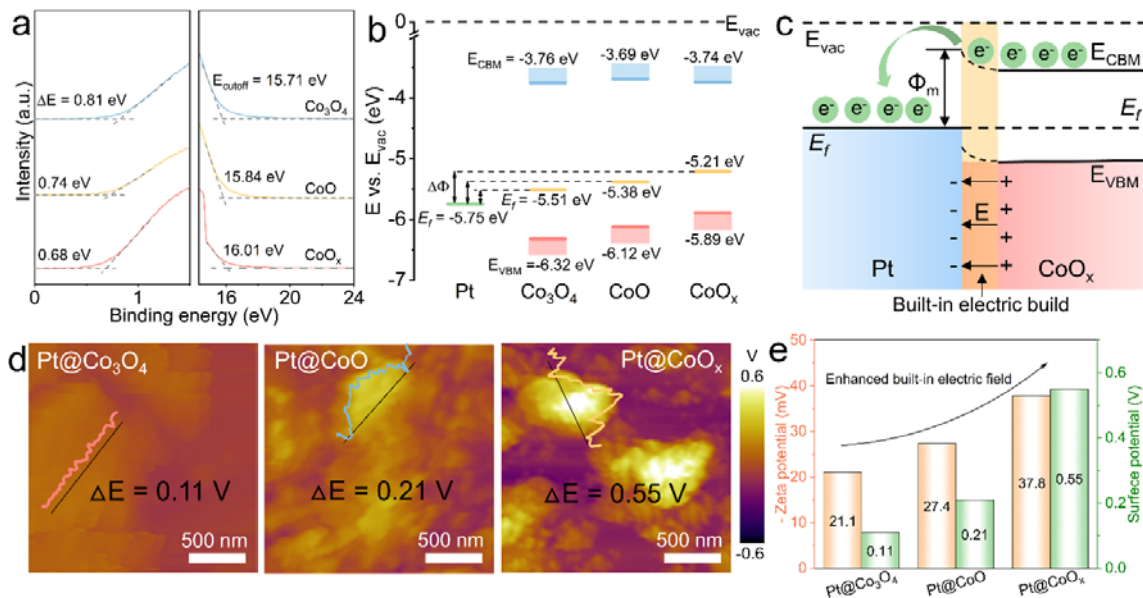
Figure 3. (a) UPS spectra and (b) energy-band alignment diagram of CoO, CoO$_x$, and Co$_3$O$_4$ with respect to Pt. (c) Schematic illustration of the Schottky junction. (d) Surface potentials of Pt-based electrocatalysts measured by KPFM. (e) Comparison of zeta potentials and surface potentials of Pt@Co$_3$O$_4$, Pt@CoO, and Pt@CoO$_x$.

To further verify the influence of Φ on BEF, ultraviolet photoelectron spectroscopy (UPS) characterization was conducted to explore the surface electronic property (see details in Supporting Information). The specific values are concluded in **Table S4**. As shown in **Figures 3a and S15,** the Φ value of CoO$_x$ is decreased by 0.30 eV compared with Co$_3$O$_4$, indicating an increased Fermi level. The band gaps of Co$_3$O$_4$, CoO, and CoO$_x$ were also measured by ultraviolet-visible spectroscopy (UV-vis), as shown in **Figure S16**. The CoO$_x$ reveals the smallest band gap of 2.15 eV, confirming faster charger transfer across the Fermi level. Based on these results, a comprehensive energy-band diagram is given in **Figure 3b**. Three main trends can be extracted following the sequence from Co$_3$O$_4$, CoO to CoO$_x$ (left to right): (1) the Fermi level is increased from -5.51 to -5.21 eV; (2) the ΔΦ between metal (Pt) and support (cobalt oxide) is increased from 0.24 to 0.54 eV and (3) the band gap between valence band

maximum (VBM) and conduction band minimum (CBM) is decreased from 2.56 to 2.15 eV. It is pertinent to remark that, when metal is put in direct contact with a semiconductor, the large difference in Φ constructs a Schottky junction, and the $\Delta\Phi$ would drive the charge flow from high level to low until the system reaches an equilibrium.[16a, 25] Consequently, the electrons in cobalt oxide flow into Pt, leaving the positively ionized donor behind. Accordingly, a BEF is constructed with the direction from cobalt oxide to Pt.[26] It is reasonable to infer that the Pt@CoO$_x$ possesses the strongest BEF due to the largest $\Delta\Phi$. As illustrated in **Figure 3c**, the electrons flow from CoO$_x$ to Pt to reach the same Fermi level. Due to the thick space-charge layer in CoO$_x$ (caused by the relatively low electron density as compared with Pt),[27] the potential difference mainly exists in the CoO$_x$ side, bending the surficial bands of CoO$_x$ (highlighted in yellow range). Consequently, the Fermi level and CBM in bulk decrease together until they reach the same level. The bending of bands creates a Schottky barrier with a height of Φ_m, showing rectification characteristics.[27a] Thus, the single-way electron emission and charge fluctuation can effectively modulate the charge separation, which in turn, promoting the hydrogen and hydroxide adsorption processes.

Given the enlarged trend of $\Delta\Phi$ among Co$_3$O$_4$, CoO, and CoO$_x$ with respect to Pt, the BEF is anticipated to be largely influenced. To affirm this assertion, the surface and Zeta potential of Pt@Co$_3$O$_4$, Pt@CoO, and Pt@CoO$_x$ were measured. According to Poisson's equation-derived Kanata model[28] and previous work,[29] the magnitude of BEF can be indexed to surface potential and charge density (see details in Supporting Information). The surface potential was measured by Kelvin Probe Force Microscopy (KPFM), as shown in **Figure 3d** and **Figure S17**. The Pt@CoO$_x$ reveals the largest surface potential ($\Delta E = 0.55$ V) as compared with Pt@Co$_3$O$_4$ (0.11 V) and Pt@CoO (0.21 V). On the other hand, the charge density can be calculated by measuring the Zeta potential. As shown in **Figure 3e**, the Zeta potential of Pt@CoO$_x$ (-37.8 mV) was also higher than that of Pt@Co$_3$O$_4$ (-21.1 mV) and Pt@CoO (-27.4 mV).

Subsequently, the BEF of Pt@CoO$_x$ is calculated to be 2.99 and 1.90 times enhanced than that of Pt@Co$_3$O$_4$ and Pt@CoO, respectively. Taken together, it can be inferred that the value of BEF is increased with the enlargement of ΔΦ. Additionally, the enhanced BEF is speculated to largely influence the charge redistribution, which in turn, regulates the hydrogen or hydroxide adsorption processes.
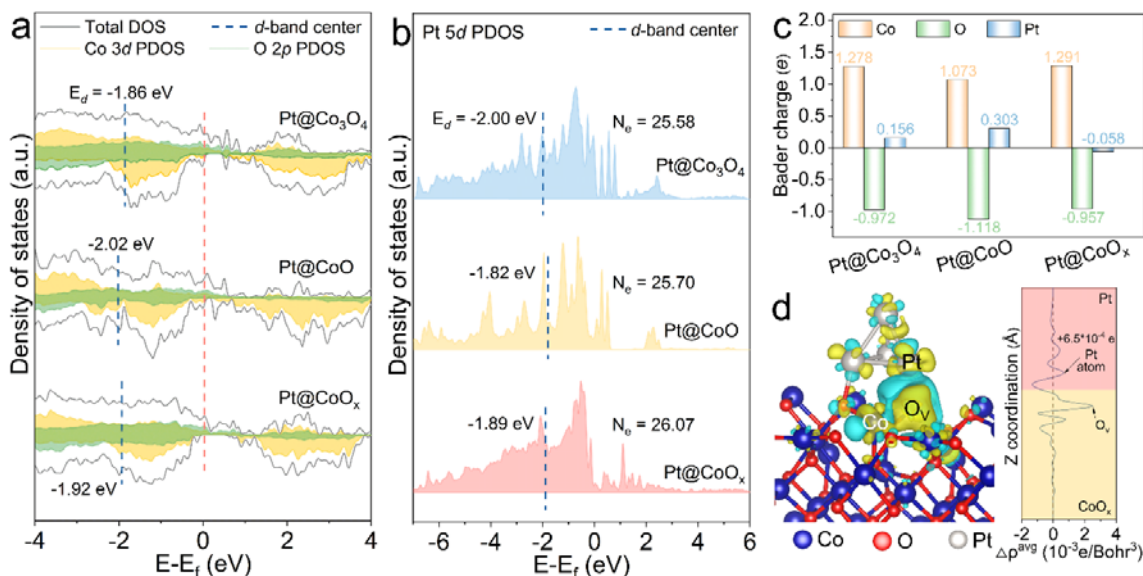
Figure 4. (a) DOS plots of Pt@Co$_3$O$_4$, Pt@CoO, and Pt@CoO$_x$. The Fermi level and Co d-band center are also highlighted. (b) Comparison of PDOS of Pt d-band for Pt@Co$_3$O$_4$, Pt@CoO, and Pt@CoO$_x$. (c) Computed Bader charges of Co, O, and Pt atoms in Pt@Co$_3$O$_4$, Pt@CoO, and Pt@CoO$_x$. (d) Isosurfaces of charge density difference (left) and planar-average charge density plot (right) of Pt@CoO$_x$. Yellow and cyan clouds indicate charge gain and loss, respectively. The isosurface is 0.002 e Bohr^{-3}.

To further explore the effects of BEF on the electronic structure across the interface, density functional theory (DFT) calculations were performed to systematically reveal the electron migration, Pt nanoparticles anchored on different cobalt oxide supports were adopted as models (**Figure S18**). As compared with the cobalt oxides, which show semiconductor nature (**Figure 3b**), the integrated densities of states (DOS) for all the three Pt-based electrocatalysts cross over the Fermi level (**Figure 4a**), verifying the constructed metal-support interface and much enhanced electron transfer. Additionally, the Pt@CoO$_x$ exhibits a moderate Co d-band center of -1.92 eV, as the Co d-band center is supposed to correlate with the hydroxide adsorption

strength,[22a, 30] the intermediate value may indicate a mild adsorption/desorption process. On the other hand, the projected DOS (PDOS) of Pt $5d$ are also compared (**Figure 4b**). The convoluted Pt d-band center of Pt@CoO$_x$ is -1.89 eV. According to the d-band center theory,[31] an ideal binding energy should be neither strong nor weak, and the binding energy between adsorbate and adsorbent is strongly correlated with the highly localized metal d states. Naturally, the d-band center of pure Pt ($\sim$ -1.93 eV) is considered as a benchmark.[32] Since the Pt d-band center in Pt@CoO$_x$ is most close to the ideal position, the optimized d-band filling suggests moderate binding energies.

Meanwhile, the total occupied electrons (N_e) of Pt d-band in Pt@CoO$_x$ is counted to be the largest (26.07). Therefore, it is rational to consider that the strong BEF in Pt@CoO$_x$ drives charge transfer from Co to Pt, implying optimized adsorption energy. Such speculation is rightly verified by the Bader charge analysis (**Figure 4c**). The Co total charge gradually decreases from Pt@CoO, Pt@Co$_3$O$_4$ to Pt@CoO$_x$, demonstrating a trend of losing electrons. On the contrary, the Pt total charge increases for the same sequence, verifying charge accumulation around the Pt side. Especially, the Pt@CoO$_x$ with oxygen vacancy reveals a net negative charge as compared with Pt@Co$_3$O$_4$. These results jointly confirm the strong correlation between Co and Pt induced by the BEF and oxygen vacancy. The charge density difference and the corresponding planar-average charge density are further calculated around the oxygen vacancy, as shown in **Figure 4d**. It is shown that extra charge skews around the oxygen vacancy site, and about 6.5×10^{-4} e$^-$ flows from CoO$_x$ to Pt due to the strong BEF. Thus, the electronic analysis demonstrates the correlation interaction between Co, O, and Pt, consistent with previous results. The regulations of electron fillings in orbitals may strongly affect the binding energies of absorbates.
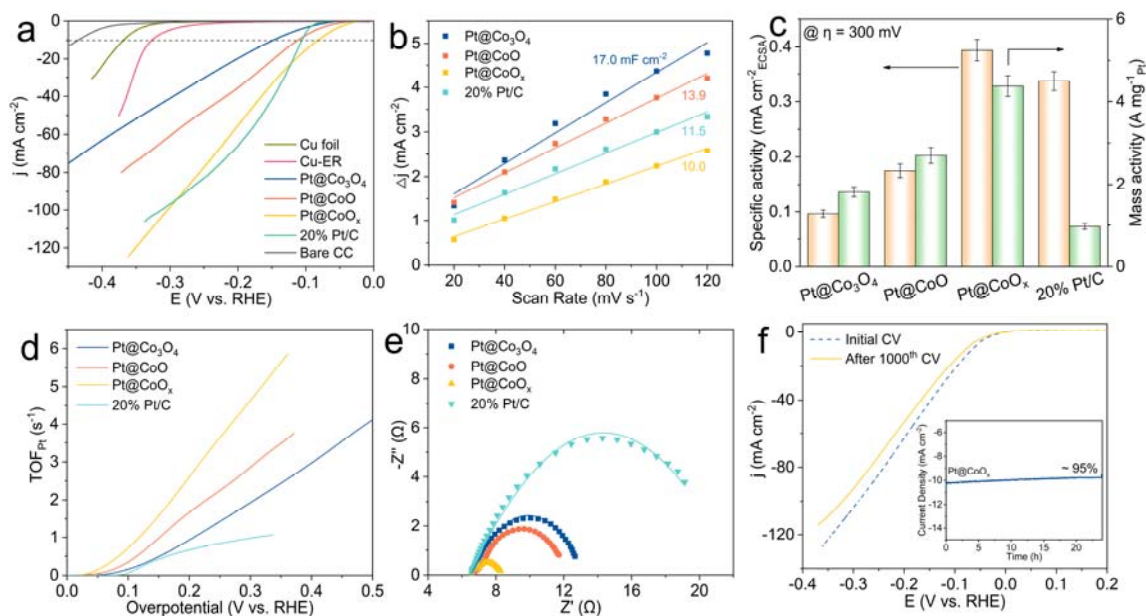
Figure 5. (a) LSV curves of as-prepared samples in H_2-saturated 1 M PBS at a scan rate of 5 mV s^{-1}. (b) C_{dl} values of Pt-based catalysts. (c) Specific activities (based on ECSA) and mass activities (based on Pt mass loading) at η = 300 mV of Pt-based catalysts. (d) TOF curves with respect to Pt atoms. (e) Nyquist plots of Pt-based catalysts at an applied potential of -0.2 V. (f) LSV curves of Pt@CoO$_x$ before and after 1000 CV cycles for stability test. Inset is 24-h chronoamperometric curve with an initial current density of ~ 10 mA cm^{-2}.

Given the electronic manipulation by the strong BEF, the intrinsic electrocatalytic activity of Pt@CoO$_x$ is anticipated to be largely influenced. To verify the speculation, HER measurements were performed in a typical three-electrode system with H_2-saturated 1 M phosphate-buffered solution (PBS) (pH ~ 7) electrolyte. The Pt@Co$_3$O$_4$, Pt@CoO, and commercial 20% Pt/C were also measured as control samples. As shown in the *i*R-corrected linear sweep voltammetry (LSV) curves (**Figure 5a**), the bare substrates (including bare CC, Cu foil and Cu-ER) demonstrate poor activity toward HER. Surprisingly, the Pt@Co$_3$O$_4$, Pt@CoO$_x$, and Pt@CoO exhibit comparable activities with 20% Pt/C at a current density of 10 mA cm^{-2} (j = 10 mA cm^{-2}). Significantly, the Pt@CoO$_x$ requires the lowest overpotential (η_{10} = 82 mV) even superior to the 20% Pt/C (η_{10} = 106 mV), demonstrating excellent activity toward neutral HER. Additionally, the polarization curve of 20% Pt/C reveals a "s" type bend due to the sluggish mass transfer, whereas the Pt@CoO$_x$ curve shows a straight linear relationship. Consequentially, the activity of Pt@CoO$_x$ prevails 20% Pt/C when the overpotential exceeds

14

~300 mV. Meanwhile, the corresponding Tafel slope (**Figure S19**) of Pt@CoO$_x$ also reveals a low value of 51.5 mV dec^{-1}, which is much smaller than that of Pt@Co$_3$O$_4$ (78.7 mV dec^{-1}) and Pt@CoO (59.8 mV dec^{-1}), confirming a preferred reaction kinetic. To further reveal the intrinsic activity of Pt-based catalysts, the electrochemical active surface areas (ECSAs) were obtained from the corresponding double-layer capacitance (C$_{dl}$) (**Figure S20**). As shown in **Figure 5b**, the Pt@CoO$_x$ exhibits the smallest C$_{dl}$ value of 10 mF cm^{-2}, which is only about half of Pt@Co$_3$O$_4$, indicating the high efficiency of the active sites. The excellent activity of Pt@CoO$_x$ is then confirmed by the ECSA- and mass-normalized column diagram, as shown in **Figure 5c**. The Pt@CoO$_x$ demonstrates the best performance among the Pt-based catalysts with a striking mass activity of 4.37 A mg^{-1}, 4.5-fold of 20% Pt/C. The outstanding catalytic activity of Pt@CoO$_x$ is superior to most of the previously reported neutral HER electrocatalysts (**Figure S21**). Moreover, the Pt-based turnover frequency (TOF) is calculated (**Figure 5d**). It is evident that the Pt@CoO$_x$ owns the highest TOF all over the potential range. Specifically, the TOF of Pt@CoO$_x$ reaches 4.64 s^{-1} at an overpotential of 300 mV, while only 1.93, 2.86, and 0.98 s^{-1} are observed for Pt@Co$_3$O$_4$, Pt@CoO, and 20% Pt/C, respectively. Electrochemical impedance spectroscopy (EIS) was also applied to investigate the charge transfer kinetics during the HER process (**Figure 5e**). The Nyquist plots were fitted by an equivalent electrical circuit (**Table S5**). The Pt@CoO$_x$ possesses the smallest charge transfer resistance of 1.8 Ω, which is much smaller than that of Pt@Co$_3$O$_4$ (6.4 Ω), Pt@CoO (5.4 Ω) and 20% Pt/C (14.7 Ω), demonstrating an improved interfacial electron transfer. The faradaic efficiency (FE) is also measured to be ~ 99%, as presented in **Figure S22**. Long-term stability is a crucial parameter to evaluate the application potential. As shown in **Figure 5f**, the Pt@CoO$_x$ maintains ~95% current density after 24 h's operation, verifying the outstanding durability. In addition, the LSV curve is only slightly anodic shifted for 29 mV to reach a large current density of 100 mA cm^{-2} after 1000's cycling. Moreover, as given in **Figure S23**, the

Pt@CoO$_x$ also reveals good HER activity in simulated seawater with a low overpotential of 423 mV at a current density of 100 mA cm^{-2}, outperforming many recently reported seawater electrocatalysts.[33] The initial current density retains ~87% after 24-h continuous operation. To further evaluate the possible morphological or compositional change, the post-HER sample was examined by TEM and XPS. As shown in **Figure S24**, the CoO$_x$ nanosheet still contains Pt particles, and a lattice distance of 4.7 Å is well-indexed to the typical Co$_3$O$_4$ (111) plane, confirming the conservation of the Pt@CoO$_x$ catalyst. The oxidation state of Co, O and Pt are also unchanged as verified by XPS result (**Figure S25**).
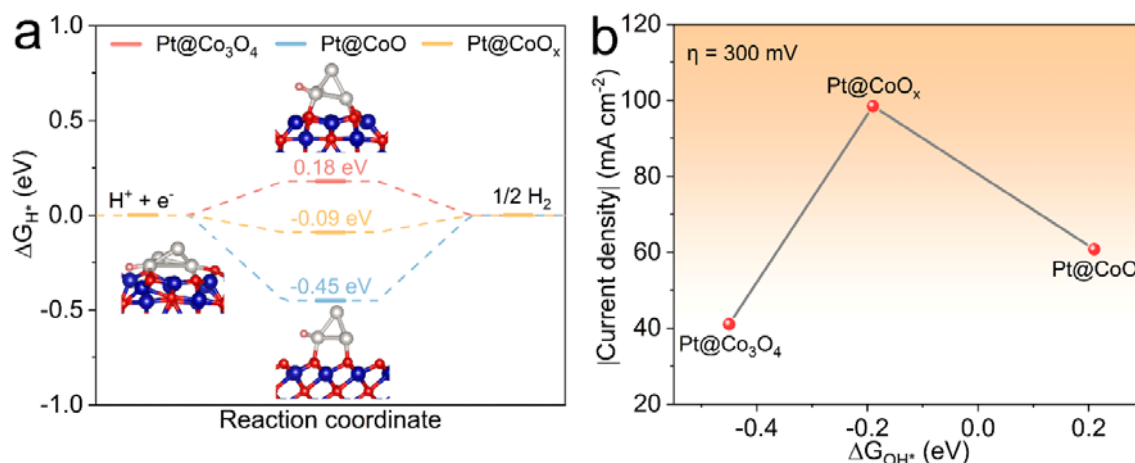
Figure 6. (a) Adsorption free energies of H* on Pt@Co$_3$O$_4$, Pt@CoO$_x$, and Pt@CoO with the corresponding models, respectively. (b) Adsorption free energies of OH* on Pt@Co$_3$O$_4$, Pt@CoO$_x$, and Pt@CoO with respect to the absolute value of experimental measured current density at η = 300 mV.

As mentioned above, the strong BEF leads to charge accumulation around the Pt site and depletion around Co and O site, which creates a biased electron flow. The modulated electron distribution is believed to affect the adsorption energies strongly. To shed more light on the catalytic nature, DFT calculation was performed to systematically screen the adsorption of reaction intermediates on different models (**Figure S26-27**). The hydrogen adsorption free energy (ΔG_{H^*}) was firstly obtained, as shown in **Figure 6a**. The Pt@CoO reveals the lowest adsorption energy of -0.45 eV. The low value demonstrates strong hydrogen adsorption, which indicates a relatively difficult desorption process. In stark contrast, the ΔG_{H^*} of Pt@Co$_3$O$_4$ is

positive, which means an unfavorable adsorption process. Compared with $Pt@Co_3O_4$, the ΔG_{H*} of $Pt@CoO_x$ is significantly reduced from 0.18 to -0.09 eV, demonstrating a moderate adsorption strength, consistent with the calculated d-band center result. It is noted that, for neutral HER, the role of hydroxide is indispensable. Previous research investigated the role of hydroxide in determining the HER reaction kinetics.[34] Accordingly, the relationship between the hydroxide adsorption free energy (ΔG_{OH*}) and HER activity is plotted (**Figure 6b**). Interestingly, a non-linear relation is obtained from experimentally measured HER activity as a function of the calculated ΔG_{OH*}, of which $Pt@CoO_x$ rises on the top. The relationship indicates an optimal value of ΔG_{OH*}, which should be slightly negative. This result is consistent with Koper's theory that points out the role of hydroxide on HER.[7a] Note that due to the limited sample numbers and theoretical models, this plot is not yet a full volcano-like picture but a comparison between the three samples studied herein. This non-linear relation also verifies that the hydrogen binding strength should not be the sole descriptor to illustrate the HER activity. For a more careful consideration, it is concluded that the Pt@CoO reveals a much negative ΔG_{H*} and a positive ΔG_{OH*}, whereas the $Pt@Co_3O_4$ demonstrates a positive ΔG_{H*} and a negative ΔG_{OH*}. The biased adsorption energy may hinder either the hydrogen or hydroxide desorption process, causing the site-blocking effect. Specifically, on the too-strong binding site, the reaction kinetic is impeded due to the sluggish desorption step; on the too-weak binding site, the reactant (H^*) is not efficiently produced. In this regard, the constructed $Pt@CoO_x$ interface with the strongest BEF reveals optimal hydrogen and hydroxide adsorption free energies, in accordance with the experimental activity results. Therefore, based on both experimental results and theoretical calculations, we conclude that a reasonable catalyst design should consider both the reactant (H^*) and other key intermediates (*e.g.*, OH^*) along the reaction pathway.

Conclusion

In summary, to overcome the slow reaction kinetics in neutral HER, we present a sacrificial agent strategy to control the oxidation state of cobalt due to different oxygen affinities. Additionally, by modulating the variation in work function, a metal-support interface is constructed with strong BEF. As a result, the charge allocation is precisely modulated as confirmed by both spectroscopic measurements and DFT calculations, which significantly influences catalytic activity. The as-prepared Pt@CoO$_x$ catalyst exhibits outstanding HER activity with a high mass activity of 4.37 A mg$^{-1}_{Pt}$ which is 4.5-fold higher than 20% Pt/C. Experimental results combined with theoretical calculation revealed the $\Delta\Phi$-induced strong BEF leads to optimized ΔG_{H*} and ΔG_{OH*}, thereby promoting neutral HER kinetics. A non-linear relationship between ΔG_{OH*} and HER activity was acquired based on variable models, demonstrating that hydroxide adsorption is one of the essential descriptors governing the neutral HER performance. We hope that our rational approach can shed light on the design principles of electrocatalysts for neutral HER and further promote the realization of practical green energy utilization.

Competing interests

The authors declare no competing interests.

References

[1] Z. W. Seh, J. Kibsgaard, C. F. Dickens, I. Chorkendorff, J. K. Nørskov, T. F. Jaramillo. *Science* **2017**, *355*, eaad4998.

[2] a) S. L. Zhang, X. F. Lu, Z. P. Wu, D. Luan, X. W. Lou. *Angew. Chem. Int. Ed.* **2021**, *60*, 19068-19073; b) X. Kong, Q. Gao, S. Bu, Z. Xu, D. Shen, B. Liu, C. S. Lee, W. Zhang. *Mater. Today Energy* **2021**, *21*, 100784; c) L. Lv, Y. Chang, X. Ao, Z. Li, J. G. Li, Y. Wu, X. Xue, Y. Cao, G. Hong, C. Wang. *Mater. Today Energy* **2020**, *17*, 100462.

[3] H. Zhang, W. Zhou, X. F. Lu, T. Chen, X. W. Lou. *Adv. Energy Mater.* **2020**, *10*, 2000882.

[4] W. Cheng, H. Zhang, D. Luan, X. W. D. Lou. *Sci. Adv.* **2021**, *7*, eabg2580.

[5] Y. Zheng, Y. Jiao, A. Vasileff, S. Z. Qiao. *Angew. Chem. Int. Ed.* **2018**, *57*, 7568-7579.

[6] a) R. Subbaraman, D. Tripkovic, D. Strmcnik, K. C. Chang, M. Uchimura, A. P. Paulikas, V. Stamenkovic, N. M. Markovic. *Science* **2011**, *334*, 1256-1260; b) Y. I. Ledezma, W. D. Z. Wallace, P. P. Sebastián, V. Climent, J. M. Feliu, M. T. Koper. *Nat. Energy* **2017**, *2*, 17031.

[7] a) I. T. McCrum, M. T. Koper. *Nat. Energy* **2020**, *5*, 891-899; b) J. Kim, H. Jung, S. M. Jung, J. Hwang, D. Y. Kim, N. Lee, K. S. Kim, H. Kwon, Y. T. Kim, J. W. Han. *J. Am. Chem. Soc.* **2020**, *143*, 1399-1408.

[8] H. Yin, S. Zhao, K. Zhao, A. Muqsit, H. Tang, L. Chang, H. Zhao, Y. Gao, Z. Tang. *Nat. Commun.* **2015**, *6*, 6430.

[9] Z. J. Chen, G. X. Cao, L. Y. Gan, H. Dai, N. Xu, M. J. Zang, H. B. Dai, H. Wu, P. Wang. *ACS Catal.* **2018**, *8*, 8866-8872.

[10] Z. W. Wei, H. J. Wang, C. Zhang, K. Xu, X. L. Lu, T. B. Lu. *Angew. Chem. Int. Ed.* **2021**, *60*, 16622-16627.

[11] D. Wang, Z. P. Liu, W. M. Yang. *ACS Catal.* **2018**, *8*, 7270-7278.

[12] a) A. Brown, D. Bradley, J. Burroughes, R. Friend, N. Greenham, P. Burn, A. Holmes, A. Kraft. *Appl. Phys. Lett.* **1992**, *61*, 2793-2795; b) G. Morello, D. F. Sala, L. Carbone, L. Manna, G. Maruccio, R. Cingolani, D. M. Giorgi. *Phys. Rev. B* **2008**, *78*, 195313; c) J. Müller, J. Lupton, P. Lagoudakis, F. Schindler, R. Koeppe, A. Rogach, J. Feldmann, D. Talapin, H. Weller. *Nano Lett.* **2005**, *5*, 2044-2049.

[13] Y. Guo, W. Shi, Y. Zhu. *EcoMat* **2019**, *1*, e12007.

[14] J. Yao, W. Huang, W. Fang, M. Kuang, N. Jia, H. Ren, D. Liu, C. Lv, C. Liu, J. Xu. *Small Methods* **2020**, *4*, 2000494.

[15] D. Cahen, A. Kahn. *Adv. Mater.* **2003**, *15*, 271-277.

[16] a) J. Li, J. Hu, M. Zhang, W. Gou, S. Zhang, Z. Chen, Y. Qu, Y. Ma. *Nat. Commun.* **2021**, *12*, 3502; b) T. Ma, R. Jacobs, J. Booske, D. Morgan. *APL Mater.* **2020**, *8*, 071110.

[17] a) X. Li, C. W. Magnuson, A. Venugopal, R. M. Tromp, J. B. Hannon, E. M. Vogel, L. Colombo, R. S. Ruoff. *J. Am. Chem. Soc.* **2011**, *133*, 2816-2819; b) X. Li, W. Cai, J. An, S. Kim, J. Nah, D. Yang, R. Piner, A. Velamakanni, I. Jung, E. Tutuc. *Science* **2009**, *324*, 1312-1314.

[18] W. Zhang, X. Wen, S. Yang, Y. Berta, Z. L. Wang. *Adv. Mater.* **2003**, *15*, 822-825.

[19] A. T. Murdock, C. D. Van Engers, J. Britton, V. Babenko, S. S. Meysami, H. Bishop, A. Crossley, A. A. Koos, N. Grobert. *Carbon* **2017**, *122*, 207-216.

[20] a) H. Han, C. Lee, Y. Kim, J. Lee, R. Kim, J. Kim, B. Yoo. *Appl. Surf. Sci.* **2021**, *550*, 149337; b) Y. Han, K. C. Lai, L. A. Rosales, M. C. Tringides, J. W. Evans, P. A. Thiel. *Surf. Sci.* **2019**, *685*, 48-58.

[21] a) Y. Liu, Y. Ying, L. Fei, Y. Liu, Q. Hu, G. Zhang, S. Y. Pang, W. Lu, C. L. Mak, X. Luo. *J. Am. Chem. Soc.* **2019**, *141*, 8136-8145; b) Y. Fang, Z. Liu, J. Han, Z. Jin, Y. Han, F. Wang, Y. Niu, Y. Wu, Y. Xu. *Adv. Energy Mater.* **2019**, *9*, 1803406.

[22] a) D. He, X. Song, W. Li, C. Tang, J. Liu, Z. Ke, C. Jiang, X. Xiao. *Angew. Chem. Int. Ed.* **2020**, *59*, 6929-6935; b) Z. Xiao, Y. C. Huang, C. L. Dong, C. Xie, Z. Liu, S. Du, W. Chen, D. Yan, L. Tao, Z. Shu. *J. Am. Chem. Soc.* **2020**, *142*, 12087-12095.

[23] a) W. Roth. *J. Phys. Chem. Solids* **1964**, *25*, 1-10; b) D. Scheerlinck, S. Hautecler. *Phys. Status Solidi B* **1976**, *73*, 223-228.

[24] a) Y. Xie, J. Cai, Y. Wu, Y. Zang, X. Zheng, J. Ye, P. Cui, S. Niu, Y. Liu, J. Zhu. *Adv. Mater.* **2019**, *31*, 1807780; b) M. A. Matin, E. Lee, H. Kim, W. S. Yoon, Y. U. Kwon. *J. Mater. Chem. A* **2015**, *3*, 17154-17164.

[25] R. T. Tung. *Appl. Phys. Rev.* **2014**, *1*, 011304.

[26] W. Mönch. *Surf. Sci.* **1994**, *299*, 928-944.

[27] a) C. A. Mead. *Solid State Electron.* **1966**, *9*, 1023-1033; b) J. Bardeen. *Phys. Rev.* **1947**, *71*, 717-727.

[28] K. Takashi, M. Masayuki, T. Hideyuki, H. Yoshihiro. **1990**, In *Modulation Spectroscopy.* 1286, pp. 56-65.

[29] a) J. Li, L. Cai, J. Shang, Y. Yu, L. Zhang. *Adv. Mater.* **2016**, *28*, 4059-4064; b) Z. Zhang, X. Chen, H. Zhang, W. Liu, W. Zhu, Y. Zhu. *Adv. Mater.* **2020**, *32*, 1907746; c) J. Jing, J. Yang, Z. Zhang, Y. Zhu. *Adv. Energy Mater.* **2021**, *11*, 2101392.

[30] H. Lee, O. Gwon, K. Choi, L. Zhang, J. Zhou, J. Park, J. W. Yoo, J. Q. Wang, J. H. Lee, G. Kim. *ACS Catal.* **2020**, *10*, 4664-4670.

[31] J. K. Nørskov, F. Studt, F. Abild Pedersen, T. Bligaard, in *Fundamental concepts in heterogeneous catalysis*. John Wiley & Sons **2014**, pp. 114-129.

[32] C. Wei, Y. Sun, G. n. G. Scherer, A. C. Fisher, M. Sherburne, J. W. Ager, Z. J. Xu. *J. Am. Chem. Soc.* **2020**, *142*, 7765-7775.

[33] a) X. Wu, S. Zhou, Z. Wang, J. Liu, W. Pei, P. Yang, J. Zhao, J. Qiu. *Adv. Energy Mater.* **2019**, *9*, 1901333; b) I. W. P. Chen, C. H. Hsiao, J. Y. Huang, Y. H. Peng, C. Y. Chang. *ACS Appl. Mater. Interfaces* **2019**, *11*, 14159-14165; c) X. Lu, J. Pan, E. Lovell, T. H. Tan, Y. H. Ng, R. Amal. *Energy Environ. Sci.* **2018**, *11*, 1898-1910.

[34] a) D. Strmcnik, P. P. Lopes, B. Genorio, V. R. Stamenkovic, N. M. Markovic. *Nano Energy* **2016**, *29*, 29-36; b) R. Subbaraman, D. Tripkovic, K. C. Chang, D. Strmcnik, A. P. Paulikas, P. Hirunsit, M. Chan, J. Greeley, V. Stamenkovic, N. M. Markovic. *Nat. Mater.* **2012**, *11*, 550-557.

Entry for the Table of Contents
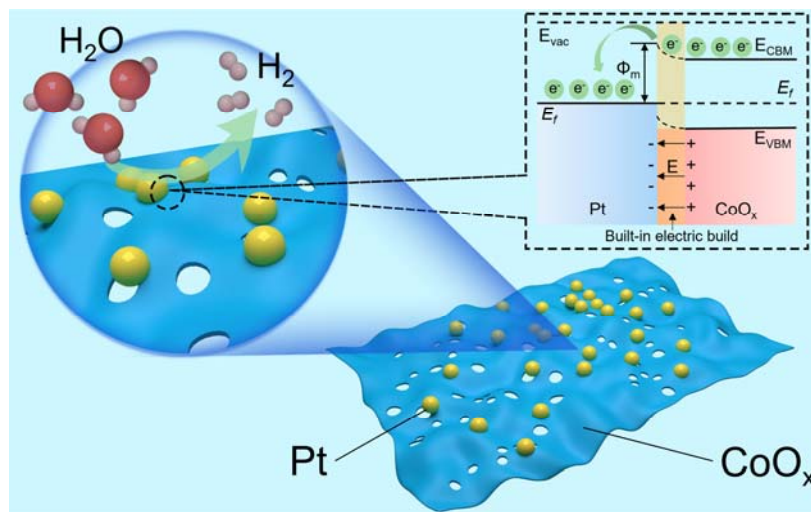
The metal-support interaction between Pt and CoO$_x$ creats strong built-in electric field across the interface and modulated the charge distribution, thus subtly optimized both hydrogen and hydroxide adsorption energy, boosting the hydrogen evolution reaction in neutral media.